TTP17-008

Top-Flavoured Dark Matter in Dark Minimal Flavour Violation

Monika Blanke, Simon Kast

Institut fur Kernphysik, Karlsruhe Institute of Technology,
Hermann-von-Helmholtz-Platz 1, D-76344 Eggenstein-Leopoldshafen, Germany

Institut fur Theoretische Teilchenphysik, Karlsruhe Institute of Technology,
Engesserstraße 7, D-76128 Karlsruhe, Germany

Abstract

We study a simplified model of top-flavoured dark matter in the framework of Dark Minimal Flavour Violation. In this setup the coupling of the dark matter flavour triplet to up-type quarks constitutes the only new source of flavour and CP violation. The parameter space of the model is restricted by LHC searches with missing energy final states, by neutral D meson mixing data, by the observed dark matter relic abundance, and by the absence of signal in direct detection experiments. We consider all of these constraints in turn, studying their implications for the allowed parameter space. Imposing the mass limits and coupling benchmarks from collider searches, we then conduct a combined analysis of all the other constraints, revealing their non-trivial interplay. Especially interesting is the combination of direct detection and relic abundance constraints, having a severe impact on the structure of the dark matter coupling matrix. We point out that future bounds from upcoming direct detection experiments, such as XENON1T, XENONnT, LUX-ZEPLIN, and DARWIN, will exclude a large part of the parameter space and push the DM mass to higher values.

Contents

1 Introduction

The evidence for dark matter (DM) collected in the past decades is overwhelming. Astronomical observations of velocity curves of stars in galaxies, as well as galaxy movements in clusters and gravitational lensing effects demand the presence of hidden sources of gravitational interactions [1–3], with new particles being the best explanation for these observations [4]. The presence of DM can not only account for astronomical observations, but also provides an elegant mechanism to explain the enhanced structure formation in the early universe [5]. Furthermore a possible interaction with SM particles (aside from gravity) serves to explain the similar orders of magnitude of baryonic ($\approx 4.9\%$) and dark matter ($\approx 26.8\%$) content in the Universe [6].

WIMP (weakly interacting massive particle) candidates for DM are particularly appealing from the theoretical point of view, as these models can provide a connection between two longstanding problems of particle physics – the origin of electroweak symmetry breaking, and the origin of DM. Further support is provided by the observation that a weak scale particle with weak annihilation cross-section straightforwardly provides the correct relic abundance by means of a thermal freeze-out, known as the WIMP miracle. However in spite of their conceptual beauty, so far no experimental evidence for WIMPs has been found. The increasingly stringent constraints from direct DM detection experiments and LHC searches put simple realizations of the WIMP paradigm under severe pressure.

A possible solution to this tension is provided by the idea of flavoured DM (FDM), which proposes a flavour structure in the dark sector [7–25]. Such a flavour structure of DM allows in general for a non-trivial coupling to the SM flavour triplets of quarks or leptons. Consequently, the stringent constraints from direct detection experiments and LHC searches can be partially evaded. In addition, flavour symmetries can provide a stabilization mechanism for DM [11, 21]. In general, a flavour violating coupling constitutes a new source of both flavour and CP violation and yields new contributions to precision flavour observables. In order to not spoil the good agreement of the latter with their SM predictions, in most studies Minimal Flavour Violation (MFV) [26–28] was imposed.

More recently, however, the phenomenology of FDM models beyond MFV has been studied. The authors of [21] proposed Dark Minimal Flavour Violation (DMFV) as a minimal non-MFV framework. In DMFV, the DM coupling to quarks constitutes the only new source of flavour and CP violation beyond the SM. The flavour phenomenology is therefore significantly altered and the constraints from precision flavour data have to be taken

into account. At the same time however the number of new parameters is limited and the stability of DM remains intact. As a concrete example the DMFV hypothesis was applied to a simplified model with fermionic DM coupling to the right-handed down-type quarks via a scalar mediator. Subsequently, in [29] a simplified model of lepton-flavoured DM in the DMFV framework was considered. Note that in this case an additional symmetry is required to stabilize DM.

In this paper we use the DMFV hypothesis to construct a simplified model of top-flavoured DM. In section 2 we present the model and revisit in short the concept of DMFV. In section 3 we study the impact of collider searches on our model, and choose parameter benchmarks for our subsequent studies. Constraints from flavour experiments, the observed relic abundance, and direct detection experiments are discussed in section 4, section 5, and section 6, respectively. Then, in section 7 we discuss the combined effect of all these constraints on the parameter space of the model. Finally in section 8 we recapitulate our findings, and contemplate the prospects of future experiments for the considered model.

2 Top-Flavoured Dark Matter beyond MFV

In this section we present the model analysed in the rest of this paper. It is constructed in analogy to the model coupling to down-quark discussed in [21]. We will revisit the most important features of a simplified model of that kind.

2.1 DMFV: Simplified Model and Parametrization

Following [21], we study a simplified model of flavoured DM with the following Lagrangian:

$$\begin{aligned}\mathcal{L} &= \mathcal{L}_{\rm SM} + i\bar{\chi}\partial\!\!\!/\chi - m_\chi\bar{\chi}\chi - (\lambda_{ij}\bar{u}_{Ri}\chi_j\phi + h.c.) \\ &\quad + (D_\mu\phi)^\dagger (D^\mu\phi) - m_\phi^2\phi^\dagger\phi + \lambda_{H\phi}\phi^\dagger\phi H^\dagger H + \lambda_{\phi\phi}\left(\phi^\dagger\phi\right)^2 .\end{aligned} \tag{2.1}$$

Here, the field χ is a Dirac fermion which is a singlet under the SM gauge group, and it transforms as a triplet under a global $U(3)_\chi$ flavour symmetry. Its lightest flavour constitutes the observed DM. χ couples to the SM up-quarks via a scalar mediator ϕ carrying QCD colour and hypercharge. Employing the Dark Minimal Flavour Violation (DMFV) paradigm [21], the quark-DM coupling matrix λ is a general 3×3 complex matrix, which is assumed to be the only new source of both flavour and CP violation. The couplings $\lambda_{H\phi}$ and $\lambda_{\phi\phi}$ are mentioned for the sake of completeness, but not relevant for this study.

As in [21], we parametrize the coupling matrix as

$$\lambda = U_\lambda D_\lambda \tag{2.2}$$

with a diagonal real matrix D_λ, and U_λ consisting of three unitary matrices carrying a mixing angle and a phase each [30]:

$$D_\lambda = \mathrm{diag}(D_{\lambda,11}, D_{\lambda,22}, D_{\lambda,33})\,, \qquad D_{\lambda,ii} > 0\,, \tag{2.3}$$

$$U_\lambda = U_{23}^\lambda U_{13}^\lambda U_{12}^\lambda \tag{2.4}$$

$$= \begin{pmatrix} 1 & 0 & 0 \\ 0 & c_{23} & s_{23}e^{-i\delta_{23}} \\ 0 & -s_{23}e^{i\delta_{23}} & c_{23} \end{pmatrix} \begin{pmatrix} c_{13} & 0 & s_{13}e^{-i\delta_{13}} \\ 0 & 1 & 0 \\ -s_{13}e^{i\delta_{13}} & 0 & c_{13} \end{pmatrix} \begin{pmatrix} c_{12} & s_{12}e^{-i\delta_{12}} & 0 \\ -s_{12}e^{i\delta_{12}} & c_{12} & 0 \\ 0 & 0 & 1 \end{pmatrix}.$$

Here $c_{ij} = \cos\theta_{ij}$ and $s_{ij} = \sin\theta_{ij}$.

This ansatz implies an unbroken $\mathbb{Z}_3$ symmetry under which only the new particles χ_i and ϕ are charged. This symmetry prevents the decay of any of the new particles to pure SM final states, guaranteeing the stability of the lightest new state. For a proof of the existence of the $\mathbb{Z}_3$ symmetry, see appendix B of [21], which closely follows the argument in [11].

2.2 Mass Hierarchy in the Dark Sector

Due to the $U(3)_\chi$ flavour symmetry the masses of the different DM flavours are the same at the level of the tree-level Lagrangian, as in the DMFV framework the only sources of flavour violation are the SM Yukawa couplings and the new coupling matrix λ. Still an unavoidable source of DM mass splitting are effects from renormalization group running. In addition, in a complete model quantum corrections from additional heavy states can arise. Such corrections can in general be parametrized by

$$m_{\chi,ij} = m_\chi(\mathbb{1} + \eta\lambda^\dagger\lambda + ...)_{ij} = m_\chi(\mathbb{1} + \eta(D_{\lambda,ii})^2\delta_{ij} + ...)_{ij}\,, \tag{2.5}$$

with no summation implied in the last term. Here, η parametrizes our lack of knowledge of the full theory. Hence we will treat it as an additional parameter. The DM mass hierarchy depends both on the sign of η and the magnitude of the couplings $D_{\lambda,ii}$. To ensure convergence of this formula we demand $|\eta(D_{\lambda,ii})^2| < 0.3$ in our analysis.

2.3 Parameter Ranges

To study the effects of all phenomenological constraints, we will randomly select points of the parameter space and check whether they comply with the constraining observables. To avoid double counting in the scanned parameter-space, we take the parameters of the coupling matrix λ to lie in the following ranges:

$$\delta_{ij} \in [0, 2\pi), \qquad \theta_{ij} \in [0, \frac{\pi}{4}], \qquad D_{\lambda,ii} > 0. \tag{2.6}$$

In order to avoid a stable coloured particle ϕ, we also need to make sure that

$$m_\chi < m_\phi. \tag{2.7}$$

Due to the DM mass corrections in (2.5) this could still be insufficient to ensure fermionic DM. But, as will be discussed in more detail later, the experimental constraints favour top-flavoured DM (the DM flavour associated with the SM top-quark) and $D_{\lambda,33} > D_{\lambda,11}, D_{\lambda,22}$. A negative η allows for a simultaneous compliance of those demands and in addition makes sure that all DM mass corrections will decrease the physical m_{χ_i}. Hence, since η can be treated as a free parameter, in the study we choose $\eta < 0$.

3 Constraints from Collider Searches

In this section we take a look at the constraints from new physics (NP) searches at the LHC on the presented model. The obtained exclusion limits will help us to restrict the parameters of our model in a meaningful way for the further analysis. It has been shown in [31] that for models with a coloured t-channel mediator in a large fraction of the parameter space jets+$\not{E}_T$ searches are more constraining than monojet+$\not{E}_T$ searches. This observation has been confirmed for the case of bottom-flavoured DM in [21], where the most stringent constraints stemmed from recasting SUSY sbottom and light squark searches. We expect the same conclusions to hold also in the present case of top-flavoured DM, and therefore restrict our study to recasting searches for top squarks and first generation squarks at the LHC. The dominant contributions to these searches stem from the production and subsequent decay of the mediator ϕ.

Before proceeding with our analysis, a comment is in order concerning the choice of experimental analyses taken into account. With the rapidly increasing integrated luminosity at run 2 of the LHC, the constraints on the mass scale of new particles become increasingly stringent. Already some of the early 13 TeV analyses, using only a few fb^{-1} of data, outperformed the respective searches at 8 TeV. In the present paper, however, we considered only the constraints from run 1 of the LHC, and disregarded the recent ones from run 2, which appeared during the completion of this work. We are aware of the fact that this approach leads to an underestimate of the constraints from the LHC. In view of other limitations of our analysis, such as considering only leading order (LO) contributions to the NP production cross-sections, and assuming the final state kinematics to be the same as in the simplified SUSY models studied by the experimental collaborations, we believe that the omission of 13 TeV data is justifiable. We expect that while the bounds on the NP masses will shift with the inclusion of 13 TeV data, the overall pattern of constraints will remain unaffected. A detailed study of the constraints from run 2 of the LHC is therefore left for future work.

3.1 Production and Decay of the Mediator

Since the mediator ϕ carries colour charge, it is produced via strong interaction processes at the LHC. In addition to the pure QCD process, in parts of the parameter space also the t-channel χ exchange diagram shown in Figure 3.1a is relevant. While the QCD production cross-section is independent of the DM mass, an m_χ dependence is introduced by the t-channel χ exchange diagram. Furthermore we note that since ϕ is charged under the new $\mathbb{Z}_3$ symmetry, it can not be singly produced – its dominant production mode is as $\phi\phi^\dagger$ pairs. Also because of the $\mathbb{Z}_3$ charge, the decay of the mediator is purely governed by the interaction in Figure 3.1b.

(a) t-channel ϕ production (b) mediator decay

Figure 3.1: (a) t-channel DM exchange diagram contributing to $\phi\phi^\dagger$ production. (b) Decay of the mediator ϕ.

The relevant processes for LHC studies then are

$$pp \to \phi\phi^\dagger \to \chi_i \bar{\chi}_j q_k \bar{q}_l \,, \tag{3.1}$$

where i, j, k, l are flavour indices. Depending on the quark flavours produced in the decay of the mediator ϕ, the final state contains top quark decay products and/or light quark jets. The DM particles escape the detector and only appear as missing transverse energy. Note that for the study of collider constraints we assume the DM flavours to be degenerate. As small splittings would result in additional soft visible decay products that are difficult to search for, this approximation is justified.

3.2 Analysis of LHC Constraints

The final state signatures are then the same as in searches for supersymmetric squarks already conducted at the LHC. The production of a stop anti-stop pair yields a $t\bar{t} + \not{E}_T$ signature, while the production and decay of squarks of the first or second generation gives jet signals with missing transverse energy. In addition to these experimentally well-constrained channels, also the final state $tj + \not{E}_T$ is generated, similar to supersymmetric scenarios with flavour violating squark decays, see e. g. [32–37]. As no dedicated searches for this final state exists, we do not pursue it further here.

Instead, in order to get a handle on the bounds from LHC on our model, we pick two of the most constraining run 1 squark searches by ATLAS, [38] for top squarks, and [39] for first and second generation squarks, and apply the obtained cross-section limits to our model. To this end we implement our model in FeynRules [40], evaluate the LO signal cross section with MadGraph 5 [41], and compare the results with the respective exclusion limits presented in [38, 39]. In doing this we neglect the potentially different final state kinematics arising from the t-channel production process, which we deem to have a minor impact on our results. To reduce the number of free parameters, we first set the mixing angels and phases in the coupling matrix λ to zero. The influence of the mixing angles will later be discussed in more detail. Furthermore we assume a coupling degeneracy $D_{\lambda,11}{=}D_{\lambda,22}$ for simplicity.

Applying the ATLAS cross-section limits on the $t\bar{t} + \not{E}_T$ final state [38] to our model, we obtain the exclusion contours shown in Figure 3.2a for different values of $D_{\lambda,11}{=}D_{\lambda,22}$ and constant $D_{\lambda,33}{=}2.0$. We can see that for small $D_{\lambda,11}{=}D_{\lambda,22}$ the excluded mass range is relatively large and shrinks when those couplings are increased. The reason is the decrease of the branching ratio into the top final state, since the couplings of ϕ to up and charm become stronger. However we can also see that the excluded area starts to grow again, when $D_{\lambda,11}{=}D_{\lambda,22}$ grows even bigger. This effect originates in the t-channel production process becoming relevant. For large enough couplings this process exceeds the QCD production significantly. Due to the valence up quarks in the proton, it is in fact the value of $D_{\lambda,11}$ which governs the magnitude of this process. The effect can also be seen in Figure 3.2b. The $t\bar{t} + \not{E}_T$ cross-section takes the highest values for large and degenerate couplings $D_{\lambda,11}{=}D_{\lambda,22}{=}D_{\lambda,33}$, although the branching ratio into $t\bar{t} + \not{E}_T$ is only about $1/9$ in this case.

Next let us take a look at the exclusion limits obtained from the ATLAS search for the jets$+\not{E}_T$ final state [39]. In Figure 3.3a we see the excluded areas for fixed $D_{\lambda,11}{=}D_{\lambda,22}{=}2.0$ with increasing $D_{\lambda,33}$. The $\phi\phi^\dagger$ production cross-section hence only depends on the masses, but the branching ratio into the jet final state decreases with increasing $D_{\lambda,33}$. We see that for $D_{\lambda,33}{<}D_{\lambda,11}{,}D_{\lambda,22}$ the constraints nearly exclude the entire interesting parameter space. While a large mediator mass would ensure that the constraints are satisfied, in combination with the constraints from the observed relic abundance also a large DM mass would be required (see section 5). Since we do not want to preclude DM masses in the region most accessible to direct DM detection experiments, we do not pursue this option.

The red curve, $D_{\lambda,11}{=}D_{\lambda,22}{=}D_{\lambda,33}{=}2.0$, still excludes a significant region of parameter space. By taking the mediator mass to be $m_\phi{=}850$ GeV and the couplings $D_{\lambda,11}{=}D_{\lambda,22}{<}D_{\lambda,33}{\leq}$ 2.0, we can make sure that the jets $+\not{E}_T$ constraints are always fulfilled. Such a setup also allows for reasonable DM masses, as we will see later on. This choice also ensures that the $t\bar{t} + \not{E}_T$ constraints are satisfied.

Figure 3.3b illustrates the dependence of the jets $+\not{E}_T$ cross-section on the couplings

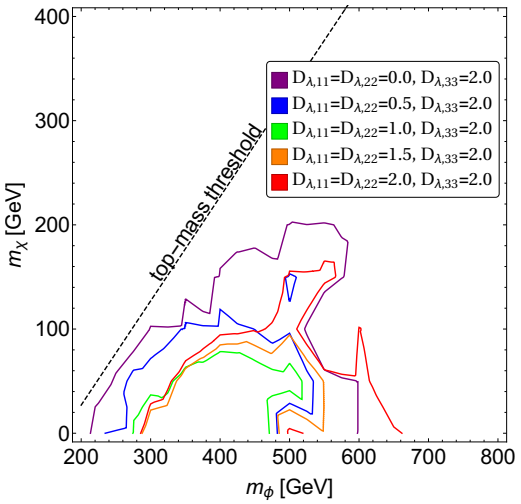

(a) 95% C.L. exclusion contours for varying first and second generation couplings.

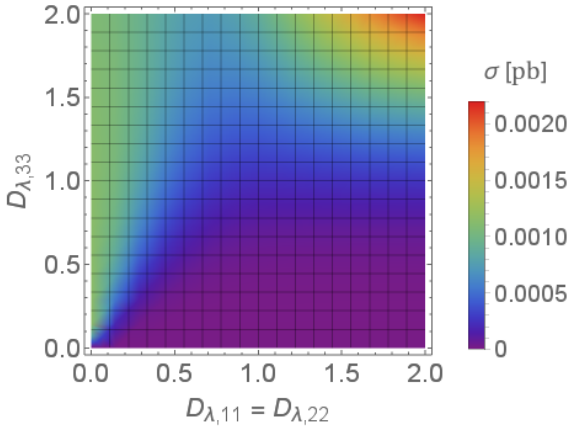

(b) LO $t\bar{t}+\not{E}_T$ cross section in 8 TeV pp collisions, for m_ϕ=850 GeV and m_χ=50 GeV.

Figure 3.2: Constraints from the $t\bar{t}+\not{E}_T$ final state at the 8 TeV LHC, obtained from [38].

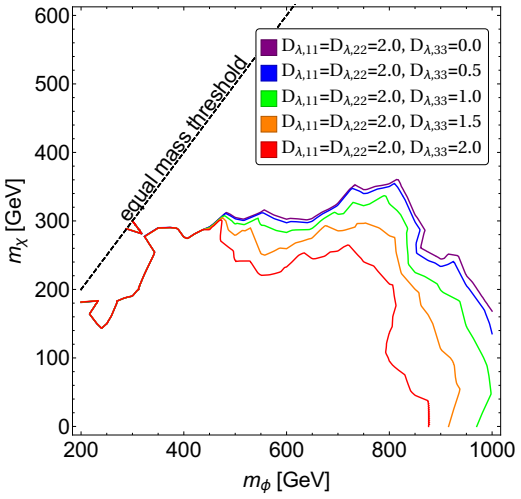

(a) 95% C.L. exclusion contours with fixed $D_{\lambda,11}$=$D_{\lambda,22}$= 2.0 and increasing $D_{\lambda,33}$.

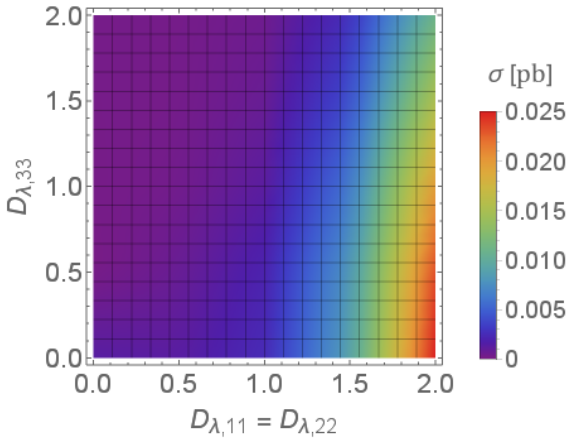

(b) LO jets $+\not{E}_T$ cross section in 8 TeV pp collisions, for m_ϕ=850 GeV and m_χ=50 GeV.

Figure 3.3: Constraints from the jets$+\not{E}_T$ final state at the 8 TeV LHC, obtained from [39].

$D_{\lambda,11}$=$D_{\lambda,22}$ and $D_{\lambda,33}$. Increasing values of $D_{\lambda,11}$=$D_{\lambda,22}$ increase the contribution of the t-channel production process. An increase in $D_{\lambda,33}$ on the other hand reduces the branching ratio of the jets + $\not{E}_T$ final state.

3.3 Impact of Flavour Mixing Angles

Non-zero flavour mixing angles in the coupling matrix λ can have a significant impact on the LHC constraints discussed above. A non-zero mixing angle θ_{ij} allows the mediator to decay into a quark q_i and a DM flavour χ_j not associated with this quark flavour. This decay is then governed by $D_{\lambda,jj}$, in contrast to the flavour conserving case where the decay into the quark q_i is always governed by $D_{\lambda,ii}$. Hence, non-zero flavour mixing effectively decreases the influence of one $D_{\lambda,ii}$ on a quark final state in favour of another, $D_{\lambda,jj}$. So if one of these couplings is quite small, while the other is at the upper end of the allowed parameter range, the effects could significantly change the branching ratio into a given final state. The t-channel production process can be affected in a similar way.

For the choice of parameter ranges we make at the end of this section, these effects raise no issue with the collider constraints. Since we impose $D_{\lambda,11}$,$D_{\lambda,22}$≤$D_{\lambda,33}$, flavour mixing will never be able to cause cross sections for jets + $\not{E}_T$ final states which are larger than in the case of $D_{\lambda,11}$=$D_{\lambda,22}$=$D_{\lambda,33}$ and hence the red exclusion line in Figure 3.3b, based on which we choose the mediator mass, remains the worst case scenario. Due to this choice, also the constraints on $t\bar{t}\not{E}_T$ are not problematic.

3.4 Summary of LHC Constraints

Summarizing the results of this section, the application of constraints from LHC searches for supersymmetric squarks yields the following information:

- The t-channel production process plays a dominant role for large couplings $D_{\lambda,11}$=$D_{\lambda,22}$.
- The most stringet constraints come from searches for jets + $\not{E}_T$ final states.
- By appropriately restricting our parameter ranges for the studies to follow, we can ensure that the constraints from LHC searches are satisfied. We choose:

$$m_\phi = 850 \text{ GeV}, \tag{3.2}$$

$$2.0 \geq D_{\lambda,33} \geq D_{\lambda,11}, D_{\lambda,22}\,. \tag{3.3}$$

  We note that the chosen value of m_ϕ might be too low to be consistent with the 13 TeV LHC data if the DM mass is small. As we will see later, however, the DM mass is bounded from below by requiring the correct relic abundance, as well as imposing the cross-section limits from direct detection experiments.

- Flavour mixing angles can in general have a significant influence on the observed cross-sections. However, our choice of parameter ranges ensures that the constraints are satisfied.

4 Flavour Constraints

By construction the DMFV framework allows the coupling matrix λ to include both flavour mixing angles and CP-violating phases and therefore in general leads to significant new flavour and CP-violating effects. In the original model with DM coupling to down-type quarks [21], strong constraints on the structure of the coupling matrix λ were derived from the measured values of $K^0 - \bar{K}^0$ and $B_{d,s} - \bar{B}_{d,s}$ mixing observables. These constraints are not relevant for the present model where DM couples to up-type quarks. Instead the only relevant constraints are obtained from $D^0 - \bar{D}^0$ mixing observables.

4.1 New Contribution to Neutral D Meson Mixing

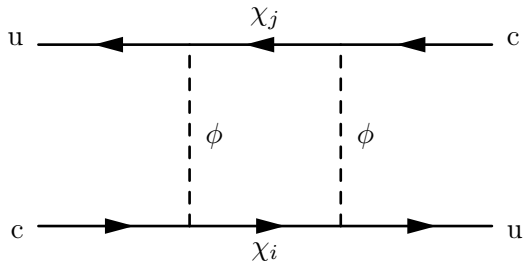

Figure 4.1: Feynman diagram for the new one-loop contribution to neutral D meson mixing

Figure 4.1 shows the leading order NP contribution to the neutral D meson mixing amplitude. Calculating the diagram and including the appropriate symmetry factor, we find the effective Hamiltonian

$$\mathcal{H}_{\text{eff}}^{\Delta C=2,\text{new}} = \frac{1}{128\pi^2 m_\phi^2} \sum_{i,j} \lambda_{ui}\lambda_{ci}^*\lambda_{uj}\lambda_{cj}^* \cdot L(x_i, x_j) \cdot Q_{uc}^{VRR} + h.c. \tag{4.1}$$

with the loop function

$$L(x_i, x_j) = \left(\frac{x_i^2 \log(x_i)}{(x_i - x_j)(1 - x_i)^2} + \frac{x_j^2 \log(x_j)}{(x_j - x_i)(1 - x_j)^2} + \frac{1}{(1 - x_i)(1 - x_j)} \right) \tag{4.2}$$

and the effective operator

$$Q_{uc}^{VRR} = (\bar{u}_\alpha \gamma_\mu P_R c_\alpha)\,(\bar{u}_\beta \gamma_\nu P_R c_\beta)\ , \tag{4.3}$$

where summation over the colour indices α, β is understood.

To obtain the NP contribution to the off-diagonal element of the $D^0 - \bar{D}^0$ mass matrix, we use the expression for the hadronic matrix element:

$$\langle \bar{D}^0 | Q_{uc}^{VRR} | D^0 \rangle = \frac{2}{3} m_D^2 f_D^2 \hat{B}_D \,, \tag{4.4}$$

from which we find

$$\begin{aligned} M_{12}^{D,\text{new}} &= \frac{1}{2m_D} \langle \bar{D}^0 | \mathcal{H}_{\text{eff}}^{\Delta C=2,\text{new}} | D^0 \rangle^* \\ &= \frac{1}{384\pi^2 m_\phi^2} \eta_D \, m_D \, f_D^2 \, \hat{B}_D \sum_{i,j} \lambda_{ui}^* \lambda_{ci} \lambda_{uj}^* \lambda_{cj} \cdot L(x_i, x_j) \,. \end{aligned} \tag{4.5}$$

The parameter η_D comprises the corrections from renormalisation group running from the weak scale $\mu \sim M_W$ to the meson scale $\mu = 3\,\text{GeV}$ [42], where the relevant lattice calculations [43, 44] are performed. Following [21], we neglect the contribution from running from the weak to the NP scale as well as differences in matching conditions between the NP scenario and the SM.

Since the new particles have significantly larger masses than the neutral D mesons, the off-diagonal element of the absorptive part of the mixing amplitude, Γ_{12}^D, is unaffected by NP.

4.2 Constraints from Neutral D Meson Mixing

Using the model-independent constraints on the $D^0 - \bar{D}^0$ mixing amplitude [46], as well as the numerical values for the other input parameters collected in Table 1, we can now constrain the parameter space of our model. Recall that the CP-violating phase Φ_{12}^D is simply the phase of M_{12}^D, when using the convention $\arg(\Gamma_{12}^D) = 0$. It is generated by the complex phases of the new coupling matrix λ.

m_{D^0}	$(1864.75 \pm 0.15 \pm 0.11)\,\text{MeV}$
$\hat{B}_D$	0.75 ± 0.02
f_D	209.2 ± 3.3 MeV
η_D	0.772
$\lvert M_{12}^D \rvert$	$(4.4 \pm 2.0) \cdot 10^{-3}\,\text{ps}^{-1}$
Φ_{12}^D	$(2.0 \pm 2.7)^\circ$

Table 1: Parameters and experimental constraints used in the numerical analysis [42–46].

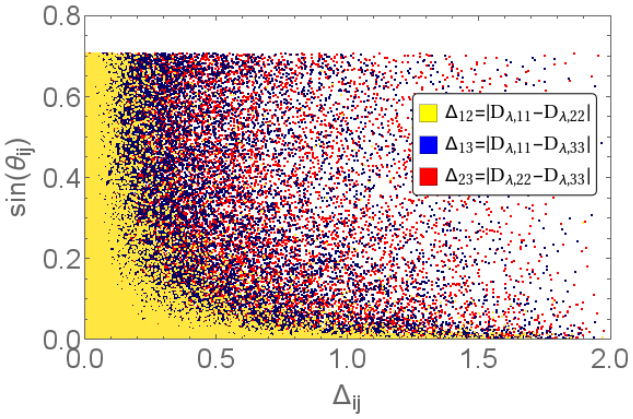

Figure 4.2: Allowed mixing angles in dependence of the splittings between couplings $D_{\lambda,ii}$, for DM mass m_χ=250 GeV and mediator mass m_ϕ=850 GeV.

Recalling the parametrization of λ from section 2 and neglecting the DM mass splittings, we can simplify the sum over the DM flavours i, j as

$$\sum_{i,j} \lambda^*_{ui}\lambda_{ci}\lambda^*_{uj}\lambda_{cj} = \Big((\lambda\lambda^\dagger)_{cu}\Big)^2 = \Big((U_\lambda D_\lambda D_\lambda^\dagger U_\lambda^\dagger)_{cu}\Big)^2 . \tag{4.6}$$

This expression gives us a good estimate of the effects of the D meson mixing constraints. Recall that D_λ is a real diagonal matrix and U_λ is a product of three unitary two-generation mixing matrices. We can see that in order to suppress the new contributions to $D^0 - \bar{D}^0$ mixing, either a near degeneracy of the couplings $D_{\lambda,11} \simeq D_{\lambda,22}$ or a small mixing angle $\theta_{12} \simeq 0$ is required. For a more detailed discussion of flavour-safe coupling scenarios in DMFV, see section 5.2 of [21].

In Figure 4.2 we see the constraints on the flavour mixing angles θ_{ij} for a specific choice of the mediator and DM mass. We observe that, as expected, the mixing angle θ_{12} is constrained to be small, unless the couplings $D_{\lambda,11}$ and $D_{\lambda,22}$ are close in value. The impact on the mixing angles θ_{13} and θ_{23}, on the other hand is minor: Only if both of these mixing angles are large, a relevant NP contribution to $D^0 - \bar{D}^0$ mixing is generated and the experimental constraints become effective. This pattern remains qualitatively the same for different values of the mediator and DM mass.

4.3 Rare Decays

In the original DMFV model with DM coupling to down-type quarks [21], the NP effects in rare K and B decays have been found to be negligible. This conclusion can be transferred to our model, yielding SM-like expectations for rare decays of D mesons.

In addition, the constraints from rare flavour violating top decays are not yet stringent enough to be relevant for our model. Consequently, flavour mixing involving the third generation remains essentially unconstrained.

One possible exception is the FCNC top-quark decay $t \to q + \text{invisible}$ with $q = u, c$. Due to the large top quark mass, for a significant range of DM masses $m_\chi < m_t/2$, the decay $t \to \chi\bar{\chi}q$ is kinematically allowed and may receive a potentially large NP contribution. However, as we will see later in more detail, such low masses are excluded by a combination of relic abundance, direct detection and collider constraints.

5 Implications of Observed Relic Abundance

About 80% of all matter in the universe is dark, while only about 20% consists of the well-studied SM particles. It is quite surprising that the order of magnitude of the matter share for SM particles and DM particles is the same. An elegant way to explain such a connection is to assume the DM abundance to be the relic of a thermal freeze-out. For the freeze-out process to yield the observed relic abundance, theoretical considerations demand the effective cross-section for a DM mass above 1 GeV to be [47]

$$\langle \sigma v \rangle_{\text{eff}} = 2.2 \times 10^{-26}\,\text{cm}^3/\text{s}. \tag{5.1}$$

We note that this constraint can be relaxed if additional stable particles contribute to the observed DM. In our numerical analysis we require the calculated value for $\langle \sigma v \rangle_{\text{eff}}$ to match the above value within a 10% tolerance range. The size of this tolerance range simplifies the numerical calculation, and we checked that the results are not affected qualitatively by this choice.

In the case of flavoured DM the freeze-out process can be significantly altered by the presence of the additional dark flavours, depending on the mass splitting in the DM sector [21]. Furthermore due to the large top-quark mass, the number of final states that are kinematically accessible is reduced for sufficiently small DM masses.

In this section we first give the general expression for the DM annihilation cross section, including the relevant phase-space factors for non-negligible top quark mass. We continue with the discussion of two special cases of freeze-out scenarios and their phenomenology.

5.1 Annihilation of Flavoured DM

Since our model includes three DM flavours, DM annihilation can proceed via several processes. Depending on the flavours present at the time of freeze-out, we need to average over the possible processes to obtain the correct annihilation cross-section. First we assume that all flavours are present and the DM mass is larger than the top quark mass, so that

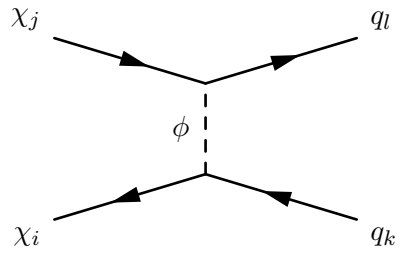

Figure 5.1: DM annihilation process at tree-level

all quark final states are kinematically allowed. Combining the procedure in [48] with the previous results from [21] (which neglected the phase-space factors due to negligible quark masses in the down-sector), we find the overall averaged annihilation cross-section

$$\langle\sigma v\rangle_{\text{eff}} = \frac{1}{18}\cdot\frac{3}{32\pi}\cdot\frac{1}{4}\sum_{i,j=1}^{3}\sum_{k,l=u,c,t}|\lambda_{ki}|^2|\lambda_{lj}|^2\,\frac{\sqrt{\left(4m_\chi^2-(m_k-m_l)^2\right)\left(4m_\chi^2-(m_k+m_l)^2\right)}}{\left(m_\phi^2+m_\chi^2-\frac{m_k^2}{2}-\frac{m_l^2}{2}\right)^2} \tag{5.2}$$

where $m_{k,l}$ are the masses of the final state quarks. Note that this formula includes a factor of $1/2$ stemming from the conversion to an effective cross-section for a Dirac fermion [49,50], as well as a flavour averaging factor of $1/9$. The DM flavours present at the time of freeze-out need to have nearly degenerate masses, hence it is safe to set $m_{\chi_i} = m_{\chi_j} = m_\chi$.

5.2 Possible Freeze-Out Scenarios

DM freeze-out occurs when the temperature drops below a critical value $T_f \approx m_\chi/20$. As discussed in section 2, in DMFV the masses of the dark flavours χ_i are split by the non-universality of the coupling matrix λ:

$$m_{ij} = m_\chi(\mathbb{1} + \eta\lambda^\dagger\lambda + ...)_{ij} = m_\chi(\mathbb{1} + \eta(D_{\lambda,ii})^2 + ...)_{ij}. \tag{2.5}$$

If the splitting is negligible compared to T_f, all flavours are present at the time of freeze-out and (5.2) gives the correct value for the annihilation cross-section. Although all flavours contribute to the freeze-out, the heavier flavours eventually decay and the presently observed DM consists of the lightest flavour only. If on the other hand the lightest flavour(s) are split significantly, the heavier flavours have decayed by the time the DM freeze-out sets in. In that case (5.2) has to be modified accordingly: the first sum then runs only over the DM flavours present at freeze-out. As already mentioned, we focus on the phenomenologically preferred case of top-flavoured DM. In section 3 we found that the LHC constraints prefer $D_{\lambda,33}$ to be the largest DM coupling. Choosing a negative η hence ensures the top-flavour to be the DM candidate.

In our analysis we study two benchmark cases:

- In the **quasi-degenerate freeze-out (QDF)** scenario we assume all flavours to be present at the time of DM freeze-out. To ensure this we demand the mass splitting to be below 1 %. For simplicity we fix $\eta = -0.01$, which is the smallest justifiable magnitude. A different choice of η changes our findings quantitatively but not qualitatively.
- In the **single flavour freeze-out (SFF)** scenario we focus on the case of the top-flavour being split significantly from the others and hence being the only flavor present at the time of freeze-out. We demand a mass splitting of at least 10% for this scenario to happen. In this case we set $\eta = -0.075$ which, for our choice $D_{\lambda,ii} \leq 2.0$, is the maximum value consistent with DM mass corrections of at most 30 %.

In addition to this discrimination of possible freeze-out scenarios, we also need to consider the case $m_\chi < m_t$. If the DM mass drops below the top mass threshold, annihilation into $t\bar{t}$ pairs is kinematically excluded. If $m_\chi < m_t/2$ also single-top final states become inaccessible. Therefore (5.2) has to be modified accordingly, affecting the constraints on the parameters of λ.

5.3 Phenomenological Analysis of Freeze-Out Scenarios

5.3.1 Quasi-Degenerate Freeze-Out

To understand the effect of the relic abundance constraints on the parameters of our model, let us first study equation (5.2) in more detail. Neglecting the phase-space factors, i. e. taking the limit $m_\chi \gg m_t$, the formula simplifies to

$$\langle \sigma v \rangle_{\text{eff}} = \frac{1}{18} \cdot \frac{3}{32\pi} \sum_{i,j=1,2,3} \frac{D_{\lambda,ii}^2 D_{\lambda,jj}^2 \cdot m_\chi^2}{\left(m_\phi^2 + m_\chi^2\right)^2}. \tag{5.3}$$

For a given pair of m_χ and m_ϕ, (5.3) reduces to a spherical constraint on the couplings, i. e.

$$D_{\lambda,11}^2 + D_{\lambda,22}^2 + D_{\lambda,33}^2 = \text{const.} \tag{5.4}$$

Since all couplings $D_{\lambda,ii}$ can be taken positive without loss of generality, we are in fact limited to 1/8 of the surface of a sphere. The constraint $D_{\lambda,ii} < 2.0$ then cuts out part of the remaining shell. Finally reinserting the phase-space factors and therefore the angular dependence deforms the sphere. What remains as allowed coupling region is hence part of this deformed sphere. Furthermore the mass splitting conditions for QDF establish a lower bound for $D_{\lambda,11}$, $D_{\lambda,22}$ in dependence of $D_{\lambda,33}$. This dependence further shapes the allowed parameter space.

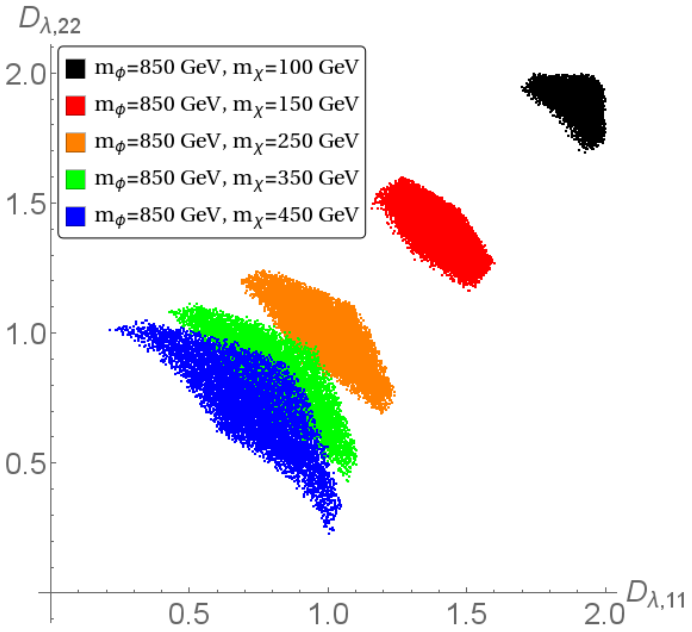

Figure 5.2: Regions of parameter space compatible with the relic abundance constraint in the QDF scenario, for different DM masses.

Figure 5.2 shows the allowed coupling range for the QDF scenario with different DM masses in the $D_{\lambda,11}$-$D_{\lambda,22}$ plane. We can clearly see the m_χ dependence of the relic abundance constraint. The smaller the DM mass gets, the larger the couplings have to be to still reach the required annihilation cross-section. This shift is more significant when m_χ drops below the top-mass threshold and then especially half the top-mass threshold. Since fewer and again fewer final states remain accessible below the respective thresholds, the total number of terms contributing to the cross-section decreases and the coupling parameters have to be even larger to compensate that. We can also see that the relic abundance constraints, together with the LHC limit of 2.0 for the couplings $D_{\lambda,ii}$, establishes a lower bound on the DM mass depending on the value of the mediator mass. The influence of the flavour mixing angles θ_{ij}, on the other hand, is insignificant for the QDF scenario.

5.3.2 Single Flavour Freeze-Out

As far as flavour mixing angles are concerned, the single flavour freeze-out (SFF) scenario is an entirely different story. Since only the top-flavour χ_t is present at the time of freeze-out, only one initial state remains in (5.2) – hence only terms involving $D_{\lambda,33}$, θ_{13} and θ_{23} contribute and the averaging factor drops out. As a result these few remaining parameters get more stringently constrained.

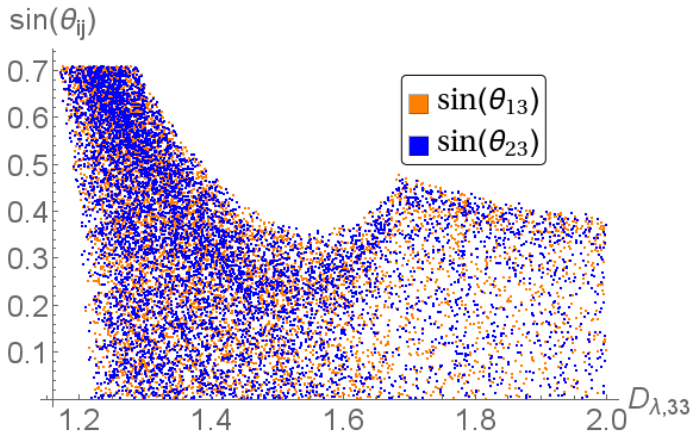

Figure 5.3: Allowed ranges for the mixing angles in dependence on $D_{\lambda,33}$, for SFF with m_ϕ=850 GeV and m_χ=220 GeV.

Figure 5.3 shows the mixing angles θ_{13} and θ_{23} as functions of $D_{\lambda,33}$ for a mediator mass of 850 GeV and a Lagrangian DM mass parameter of $m_\chi = 220$ GeV. We observe that for the smallest allowed $D_{\lambda,33}$ the mixing angles need to be maximal, in order to push the cross-section into the tolerance interval of the constraints. With increasing coupling $D_{\lambda,33}$, smaller angles are allowed as well and instead an upper bound arises. This upper bound becomes weaker when approaching the threshold value $D_{\lambda,33} \simeq 1.7$. At this point, the physical DM mass $m_{\chi_t} = m_\chi \left(1 + \eta D_{\lambda,33}^2\right)$ drops below the top quark mass, so that the annihilation channel into $t\bar{t}$ pairs becomes inaccessible. Consequently, larger flavour mixing is again required in order to enhance the DM annihilation cross-section into light flavours.

For the same reasons as in the QDF scenario we find a lower bound on the DM mass, depending on the mediator mass. But in addition, in the SFF scenario for a given value of η we also find an upper bound on the DM mass. The origin of this effect is a combination of the relic abundance constraints and the splitting condition for SFF. For a given mediator mass the combination of DM mass and the coupling parameters has to be in a certain interval. With increasing DM mass, the coupling hence has to take smaller values. At the same time the SFF condition demands $D_{\lambda,33}$ to be large enough to ensure a splitting of at least 10%, hence establishing a lower bound on $D_{\lambda,33}$ depending on η, which translates into an upper bound on the DM mass. Larger DM masses require larger values of m_ϕ and/or η.

6 Constraints from Direct Detection Experiments

In this section we discuss the constraints from direct detection experiments. The currently most stringent cross-section limits are provided by the LUX collaboration [51], which we will use in our analysis. Note that a comparable sensitivity has also been reached by PandaX-II [52]. We first discuss the relevant WIMP-nucleon interactions and study their interplay, resulting in an effective suppression of WIMP-xenon scattering. The stringent constraints on the WIMP-nucleon scattering cross-section will help us to make a case for top-flavoured DM, instead of the up or charm case.

We then turn our attention to the relative abundance of stable and quasi-stable xenon isotopes in natural xenon, which is used in experiments such as LUX. The simultaneous suppression of the respective WIMP-nucleus cross sections, necessary to keep the combined effective cross section for natural xenon in check, proves to be hard to achieve. Especially in light of future experiments, such as XENON1T [53], XENONnT [53], LUX-ZEPLIN (LZ) [54] and DARWIN [55], this will result in strong constraints on the model studied in this paper.

6.1 Relevant WIMP-Nucleon Interactions

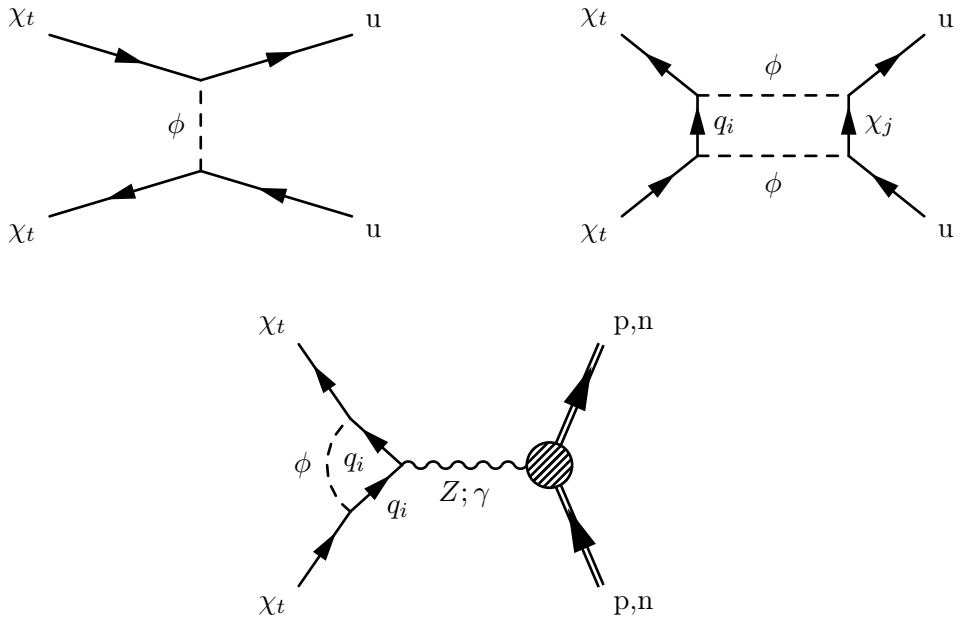

Figure 6.1: Feynman diagrams for relevant WIMP-nucleon interactions.

The relevant WIMP-nucleon scattering processes are depicted in Figure 6.1. The leading

process is the tree-level interaction, followed by contributions from box diagrams, as well as photon- and Z-penguin diagrams. In contrast to the bottom-flavoured DM model studied in [21], the Z-penguin contribution is no longer negligible, due to the large top quark mass.

The spin-independent WIMP-nucleon cross-section, for a nucleus with mass number A and atomic number Z, can be written as

$$\sigma_n^{SI} = \frac{\mu_n^2}{\pi A^2} |Z f_p + (A - Z) f_n|^2 \,, \tag{6.1}$$

with the reduced mass μ_n of the WIMP-nucleon system, and f_p and f_n parametrizing the DM couplings to the proton and neutron, respectively.

Assuming, as done throughout our analysis, that the observed DM consists solely of the top-flavour χ_t, and using the results of [13, 21], we find the following relevant contributions to f_p and f_n:

- At tree-level, DM couples to the up quarks in the nuclei via an s-channel ϕ exchange. We obtain:
$$f_p^{\text{tree}} = 2 f_n^{\text{tree}} = \frac{|\lambda_{ut}|^2}{4 m_\phi^2}. \tag{6.2}$$

- The box-diagram contribution reads
$$f_p^{\text{box}} = 2 f_n^{\text{box}} = \sum_{i,j} \frac{|\lambda_{ui}|^2 |\lambda_{jt}|^2}{32\pi^2 m_\phi^2} F\left(\frac{m_{q_i}^2}{m_\phi^2}, \frac{m_{\chi_j}^2}{m_\phi^2}\right) \,, \tag{6.3}$$
with the loop function F given in appendix C of [21].

- As the photon couples to the electric charge of the nucleon, the photon penguin diagram only contributes to f_p:
$$f_p^{\text{photon}} = -\sum_i \frac{|\lambda_{it}|^2 e^2}{48\pi^2 m_\phi^2} \left[\frac{3}{2} + \log\left(\frac{m_{q_i}^2}{m_\phi^2}\right)\right] \tag{6.4}$$

- Last but not least, the contributions from the Z penguin diagram are:
$$f_p^Z = -\frac{3|\lambda_{tt}|^2 e^2 \left(\frac{1}{2} - 2\sin^2\theta_W\right)}{32\pi^2 \sin^2\theta_W \cos^2\theta_W m_Z^2} \frac{m_t^2}{m_\phi^2} \left[1 + \log\left(\frac{m_t^2}{m_\phi^2}\right)\right] \,, \tag{6.5}$$
$$f_n^Z = -\frac{3|\lambda_{tt}|^2 e^2 \left(-\frac{1}{2}\right)}{32\pi^2 \sin^2\theta_W \cos^2\theta_W m_Z^2} \frac{m_t^2}{m_\phi^2} \left[1 + \log\left(\frac{m_t^2}{m_\phi^2}\right)\right] \,, \tag{6.6}$$
with θ_W being the weak mixing angle. It is apparent that the latter contributions are only relevant for a top quark in the loop, since otherwise the factor of m_q^2/m_ϕ^2 makes the term negligible.

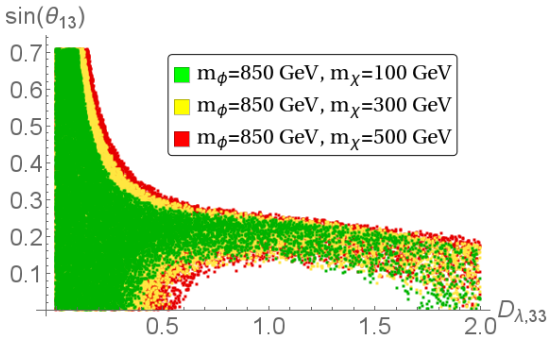

(a) Mixing angle θ_{13} as function of $D_{\lambda,33}$ for various values of m_χ and fixed m_ϕ.

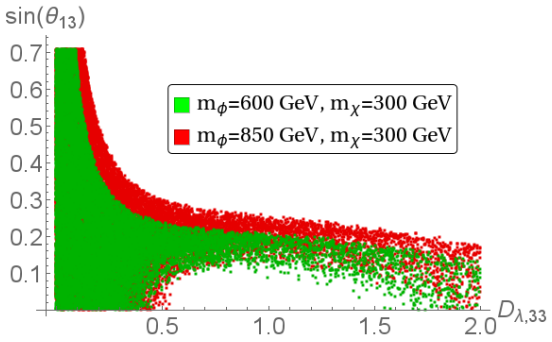

(b) Mixing angle θ_{13} as function of $D_{\lambda,33}$ for various values of m_ϕ and fixed m_χ.

Figure 6.2: Constraints on the mixing angle θ_{13} from the LUX data.

6.2 Direct Detection Constraints

The sum of all contributions to the WIMP-nucleon scattering in (6.7) has to give a cross-section below the bound provided by the LUX experiment [51]. This constraint is quite stringent for WIMP DM. A destructive interference of the various contributions, as found in [21], is therefore needed. Taking a closer look at the individual contributions we find that only the Z-penguin coupling to the neutron is negative, while all other terms in (6.7) are positive. Since the tree-level diagram in general yields the largest positive contribution, its cancellation with the Z-penguin coupling to neutrons is necessary. This required cancellation is expected to have a major influence on the shape of the allowed parameter space, when imposing the direct detection bounds.

Figure 6.2 shows the allowed region of parameter space for several values of the DM and mediator masses, with θ_{13} plotted against $D_{\lambda,33}$. We see that for small couplings $D_{\lambda,33}$ the constraints have no impact on the allowed values of θ_{13}. This comes as no surprise, since every single contribution to the WIMP-nucleon scattering is proportional to $D^2_{\lambda,33}$, so the cross-section (6.7) is proportional to $D^4_{\lambda,33}$. Sufficiently small couplings $D_{\lambda,33}$, on their own, can thus ensure that the predicted cross-section is below the LUX bound. For larger $D_{\lambda,33}$, this suppression is no longer sufficient, so that the aforementioned destructive interference between the tree-level and Z-penguin contributions is required. The tree-level contribution is proportional to $D^2_{\lambda,33}\sin^2\theta_{13}$, while the Z-penguin is proportional to $D^2_{\lambda,33}\cos^2\theta_{13}\cos^2\theta_{23}$. The latter has to cancel the tree-level (and in most cases also other sub-leading positive) contributions. The sum of those two major terms has its minimum at $\sin\theta_{13} \simeq 0.2$, as can be seen from Figure 6.2. Due to the influence of several other parameters, such as θ_{23}, we observe an allowed interval around the value of $\sin\theta_{13} = 0.2$. For values of $D_{\lambda,33}$ larger than unity, the box diagram contribution, being proportional

to $D^4_{\lambda,33}$, becomes competitive. Consequently the allowed range for θ_{13} is driven to lower values.

The necessity of this destructive interference also helps to motivate the case for top-flavoured DM. Since the nuclei consist of first generation quarks, choosing a DM associated with the second or third generation helps to suppress the tree-level contribution by a small flavour mixing angle. Furthermore the crucial negative contribution from the Z-penguin is only significant for a top-quark in the loop. Top-flavoured DM is hence favoured by the absence of signal in direct detection experiments.

As the tree level and Z-penguin diagrams yield different WIMP-nucleon copling strengths for protons and neutrons, their cancellation requires a fixed proton-to-neutron ratio in the detector material. Top-flavoured DM in DMFV therefore constitutes a concrete example of xenophobic DM [56]. A similar situation was encountered in the case of bottom-flavoured DM in DMFV, where the destructive interference arose between the box and photon penguin contributions [21].

6.3 Natural Xenon and its Isotopes

isotope	**half-life**	**abundance ρ**
^{124}Xe	stable	0.095%
^{126}Xe	stable	0.089%
^{128}Xe	stable	1.910%
^{129}Xe	stable	26.401%
^{130}Xe	stable	4.071%
^{131}Xe	stable	21.232%
^{132}Xe	stable	26.909%
^{134}Xe	stable	10.436%
^{136}Xe	2.165×10^{21} y	8.857%

Table 2: Xenon isotopes with respective half-life and natural abundance.

The LUX experiment uses natural xenon as detector material. Natural xenon consists of nine stable and quasi-stable isotopes, see Table 2). In our discussion so far we have neglected this fact and merely used an average mass number. To take into account the various isotopes, it is necessary to calculate a combined effective WIMP-nucleon cross-section for natural xenon $\sigma^{SI}_{n,\text{nat-Xe}}$, by weighting the respective cross-sections $\sigma^{SI}_{n,i}$ of the isotopes i with their relative abundance ρ_i:

$$\sigma^{SI}_{n,\text{nat-Xe}} = \sum_{i=1}^{9} \rho_i \cdot \sigma^{SI}_{n,i} = \sum_{i=1}^{9} \rho_i \cdot \frac{\mu_n^2}{\pi A_i^2} |Z f_p + (A_i - Z) f_n|^2 \,. \tag{6.7}$$

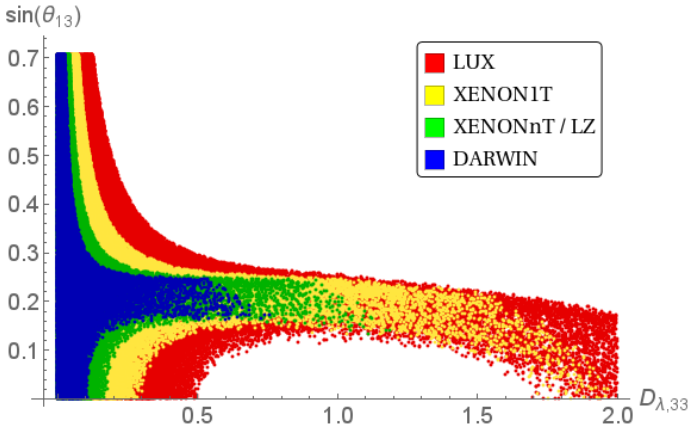

Figure 6.3: Allowed regions of parameter space, imposing the (expected) cross-section limits from present and future direct detection experiments, for DM mass m_χ=250 GeV and mediator mass m_ϕ=850 GeV.

As the cancellation between positive and negative contributions to the WIMP-nucleus scattering cross-section depends on the relative weight of f_p and f_n and hence on A_i, the cancellation will require different parameter ranges for each isotope. Since several of the xenon isotope have a significant natural abundance, the combined cross-section can only remain below the bounds from direct detection experiments if every single contribution from the different isotopes is kept sufficiently small. For this to happen simultaneously, for an increasing $D_{\lambda,33}$ an increasing amount of fine-tuning in the other parameters is necessary.

We see in Figure 6.3 that the current bounds from LUX are not stringent enough to exclude any values of $D_{\lambda,33} < 2.0$. However, future direct detection experiments such as XENON1T [53], XENONnT [53], LUX-ZEPLIN (LZ) [54] and DARWIN [55] will push the cross-section limit further down and hence make a sufficient supression of the cross-section $\sigma^{SI}_{n,\text{nat-Xe}}$ more difficult to accomplish. As we can see in Figure 6.3, already XENON1T will make the cancellation impossible for large values of $D_{\lambda,33}$, and XENONnT/LZ and DARWIN will push the upper bound on $D_{\lambda,33}$ to significantly smaller values. In the next section we will see that these findings have drastic consequences in combination with the constraints from the observed relic abundance.

7 Combined Analysis of Flavour and Dark Matter Constraints

After studying the impact of flavour, relic abundance and direct detection constraints one by one, we now turn to their combined analysis. We will see that their interplay limits the allowed region of parameter space of our model in a more stringent way.

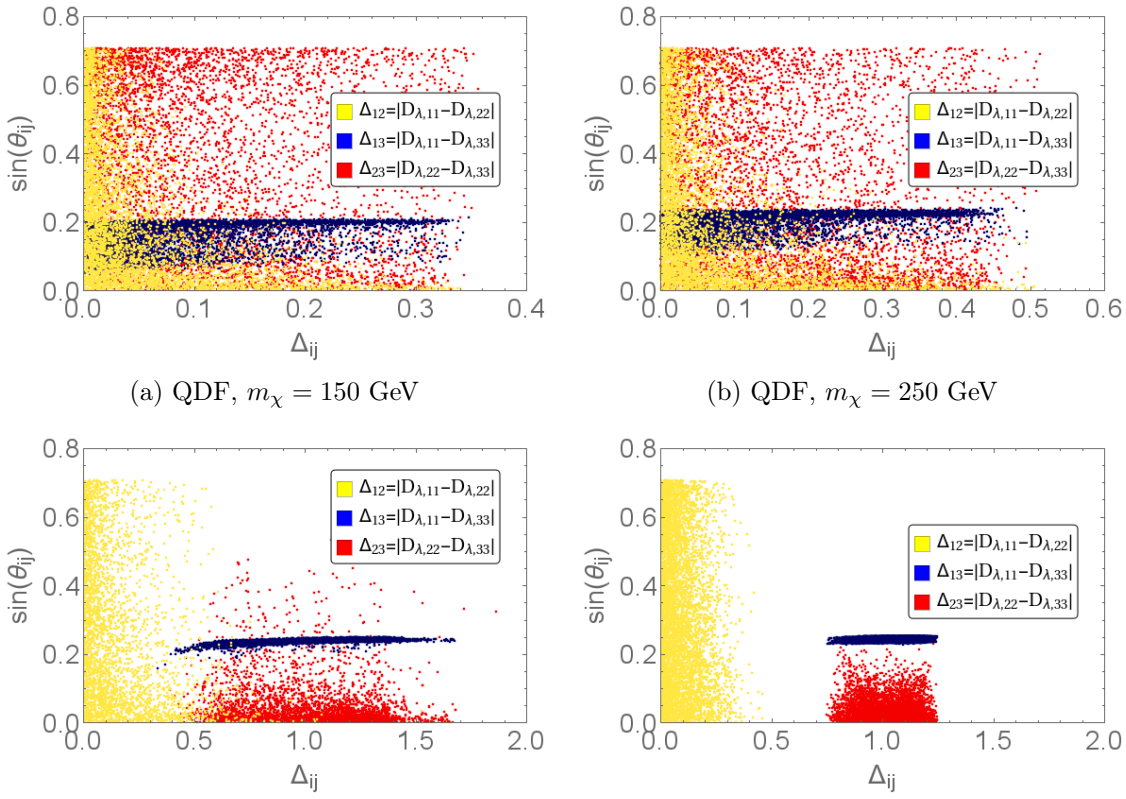

(a) QDF, $m_\chi = 150$ GeV

(b) QDF, $m_\chi = 250$ GeV

(c) SFF, $m_\chi = 225$ GeV

(d) SFF, $m_\chi = 250$ GeV

Figure 7.1: Viable regions of parameter space, imposing all constraints, for different freeze-out scenarios and DM masses, with $m_\phi = 850$ GeV.

7.1 Phenomenological Analysis

Figure 7.1 shows the effects of combining the various constraints on the allowed ranges for the mixing angles θ_{ij}, depending on the splitting between the respective couplings. In all four diagrams we recover the $D^0 - \bar{D}^0$ mixing constraint on θ_{12} – only for a small splitting between $D_{\lambda,11}$ and $D_{\lambda,22}$ large values for this mixing angle are allowed.

We also observe a strong impact on the allowed range of θ_{13}. Since a small $D_{\lambda,33}$ is excluded by the relic abundance constraint for these choices of parameters, the constraints from direct detection experiments force this mixing angle into a narrow band. The least stringent restriction on θ_{13} is found in the QDF scenario with a DM mass below the top threshold. Since for such a low DM mass, the relic abundance constraint demands a large $D_{\lambda,33}$, we are in the region where the direct detection constraints yield only a mild lower bound on θ_{13}. For larger DM masses, such as in Figure 7.1b the third generation coupling has to be

smaller and the allowed range for θ_{13} shrinks, small mixing now being excluded. An even more stringent constraint on θ_{13} can be observed in the SFF scenario. Due to the necessary splitting in the couplings, both $D_{\lambda,11}$ and $D_{\lambda,22}$ are required to be small in the presented cases. Hence the available parameter space is smaller than in the QDF case, so that θ_{13} is more stringently constrained by the LUX data.

The effects on θ_{23} are more subtle but still in some cases visible. In Figure 7.1a we see that large values for θ_{23} are slightly preferred in the QDF scenario, yielding the necessary enhancement of the annihilation cros-section. In contrast we can see that in the SFF scenario small values for θ_{23} are preferred, as in this case a reduction of the annihilation cross-section is needed.

We can furthermore observe the already mentioned consequence of demanding a significant mass splitting that leads to SFF in the transition from Figure 7.1c to Figure 7.1d. Due to the larger DM mass the relic abundance constraint reduces $D_{\lambda,33}$ and as a result also $D_{\lambda,11}$ and $D_{\lambda,22}$, thereby limiting the possible ranges for the splittings Δ_{ij}. This effect has been discussed in more detail in section 5.

To illustrate the resulting DM mass bounds, Figure 7.2 and Figure 7.3 show the allowed parameter space in the m_{χ_t}-m_ϕ-plane, again imposing all relevant flavour and DM constraints. In the SFF scenario, we observe both a lower and an upper bound on the DM mass m_{χ_t}, depending on the mediator mass. We also find that for $m_{\chi_t} < m_t$, fine-tuning is required to fulfill all constraints. The observed upper bound depends on the value of η, a parameter depending on the UV completion of the simplified model considered here. We only display the effects for one specific value, $\eta = -0,075$, but the qualitative effect will remain the same for other values.

In subsection 6.3 we found that the expected bounds from future direct detection experiments will exclude large values of $D_{\lambda,33}$. Together with the constraint from the observed DM relic abundance, which requires (for a fixed mediator mass) larger coupling values (including $D_{\lambda,33}$) for lower DM masses, this translates into a lower bound on the allowed DM masses. We can see that with improving constraints from direct detection experiments, the lower bound on the DM mass grows. In the SFF scenario, the expected cross-section limit from DARWIN would in fact exclude the whole parameter-space for the SFF scenario (with $\eta = -0,075$). Future direct detection experiments with xenon as well as other materials (with yet different cancellation patterns) are hence crucial to rule out large parts of the parameter space for top-flavoured DM – or possibly to discover it.

7.2 Summary of Constraints

To complete this section, we provide a short summary of the available constraints, as well as an overview of the consequences of their interplay.

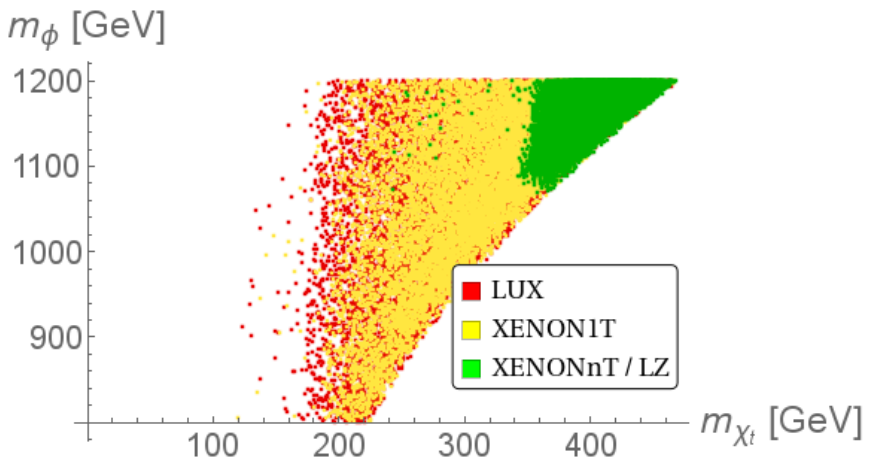

Figure 7.2: Allowed mass ranges for SFF scenario (with $\eta = -0.075$), using expected bounds from future direct detection experiments.

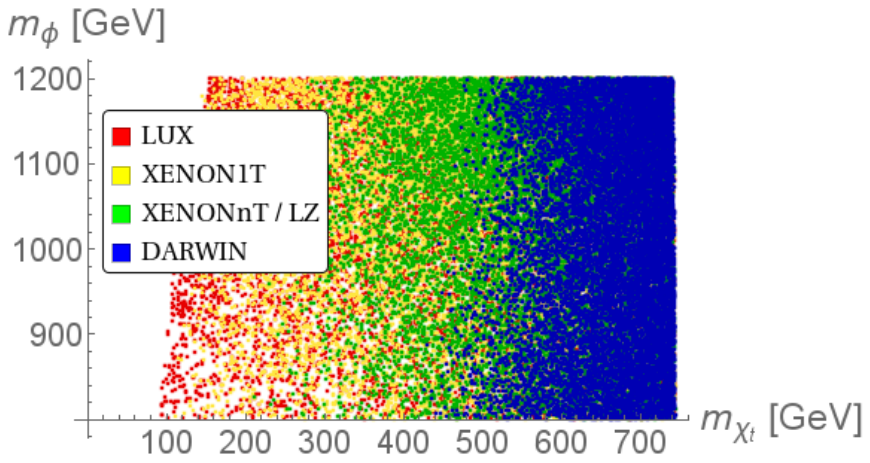

Figure 7.3: Allowed mass ranges for QDF scenario (with $\eta = -0.01$), using expected bounds from future direct detection experiments.

We identified the following crucial constraints on top-flavoured DM beyond MFV:

- The constraints from $D^0 - \bar{D}^0$ mixing requires the mixing angle θ_{12} to be small, unless the couplings $D_{\lambda,11}$ and $D_{\lambda,22}$ are nearly degenerate.
- In order to explain the observed relic abundance by a thermal DM freeze-out, the DM couplings have to lie in certain ranges (depending on the values of the mediator and DM mass).
- Due to the large top-quark mass, the mixing angles have an influence on the annihilation cross-section. This effect is sub-leading in the QDF scenario, but significant for SFF – both θ_{13} and θ_{23} considerably affect the annihilation cross-section.
- Direct detection constraints can only be fulfilled if a near-perfect cancellation of several contributions is realized. For this to happen, either the third generation coupling $D_{\lambda,33}$ has to be very small or the mixing θ_{13} has to be in a narrow band. The shape and thickness of this band depends on the other parameters of the model. This destructive interference is required for all isotopes of natural xenon present in the detector. Future direct detection experiments will therefore constrain $D_{\lambda,33}$ to lower and lower values.
- The required destructive interference in the WIMP-nucleus cross-section favours top-flavoured DM over the other cases.

Imposing all of the above constraints simultaneously, we discover their non-trivial interplay, leading to the following main conclusions:

- For the phenomenologically interesting mass ranges for χ and ϕ, the relic abundance constraints demand the coupling $D_{\lambda,33}$ to lie in a certain range. The direct detection constraints then require θ_{13} to lie in the narrow interval discussed before. The combination of relic abundance and direct detection constraints hence results in stringent bounds for θ_{13}.
- In the SFF scenario, the combination of all constraints implies DM masses $m_{\chi_t} < m_t$ to be possible only at the price of fine-tuning.
- Although we did not discuss the case of two flavours being present at the time of DM freeze-out in this paper, it is straightforward to deduce one consequence of such a scenario. Assuming that we still prefer top-flavoured DM, depending on η the dual-flavour freeze-out scenario would demand a splitting between $D_{\lambda,11}$ and $D_{\lambda,22}$. Together with the flavour constraints this would result in an upper bound on θ_{12}.
- With improving bounds from future direct detection experiments, the combination of direct detection and relic abundance constraints provides increasingly stringent lower bounds on the DM mass (depending on the value of the mediator mass).

8 Summary and Outlook

In this paper we studied a simplified model of a DM flavour triplet of Dirac fermions coupling to the SM right-handed up-quarks via a new scalar mediator (carrying the gauge charges of the up-quarks). The coupling matrix was left arbitrary, following the principle of Dark Minimal Flavour Violation [21]. We restricted our attention to the case of top-flavoured DM, which turns out to be phenomenologically preferred.

We started our analysis with estimating the constraints from LHC searches, by comparing the cross-section limits obtained in two representative run 1 searches with the predictions of our model. Assuming a WIMP DM candidate, $m_\chi \sim \mathcal{O}(100)$ GeV, we derived a lower bound on the mediator mass in conjunction with an upper bound on the DM-quark couplings. Following this result, we restricted the parameter space of the model accordingly for the rest of our analysis.

We then studied in turn the constraints from flavour violating observables, mainly neutral D meson mixing, the constraints from the assumption of DM being a thermal relic, and the bounds on the WIMP-nucleon scattering cross-section implied by direct DM detection experiments. These studies provided interesting and largely complementary constraints on the parameter space of our model. A summary of the obtained constraints can be found in subsection 7.2.

The most stringent constraints, however, were obtained when taking into account all aforementioned constraints simultaneously, revealing their non-trivial interplay. Particularly the combination of relic abundance and direct detection constraints places strong limits on the model in question. Again, details can be found in subsection 7.2.

We pointed out that the expected improved limits from upcoming direct DM detection experiments will put the scenario of top-flavoured DM under severe pressure. Experiments such as XENON1T, XENONnT, LUX-ZEPLIN (LZ), and DARWIN will hence play an essential role in either ruling out major parts of the parameter space, or in the discovery of top-flavoured DM.

Let us close with a brief comparison of our results to the ones of [21], where a simplified model of bottom-flavoured DM was studied. In the latter scenario, flavour constraints from neutral K and B meson mixings played a crucial role in constraining the flavour mixing angles of the DM-quark coupling matrix. The observed relic abundance, on the other hand, was independent of the amount of flavour mixing. Hence, while in both models strong constraints on the flavour structure of the new coupling matrix were derived, their origins differ from each other. Furthermore, both models are found to be stringently constrained by the absence of signal in direct detection experiments, so that in order to comply with the constraints, a destructive interference between various contributions was required, but the identified cancellation patterns differed from each other. Both models therefore belong

to the class of xenophobic DM models [56].

Acknowledgements We are grateful to Ulrich Nierste and José Zurita for useful discussions. S. K. acknowledges the support by the DFG-funded Doctoral School KSETA.

References

[1] P. Gorenstein and W. Tucker, *Astronomical Signatures of Dark Matter*, *Adv. High Energy Phys.* **2014** (2014) 878203.

[2] G. B. Gelmini, *TASI 2014 Lectures: The Hunt for Dark Matter*, in *Theoretical Advanced Study Institute in Elementary Particle Physics: Journeys Through the Precision Frontier: Amplitudes for Colliders (TASI 2014) Boulder, Colorado, June 2-27, 2014*, 2015. arXiv:1502.01320.

[3] K. Garrett and G. Duda, *Dark Matter: A Primer*, *Adv. Astron.* **2011** (2011) 968283, [arXiv:1006.2483].

[4] G. Bertone, D. Hooper, and J. Silk, *Particle dark matter: Evidence, candidates and constraints*, *Phys. Rept.* **405** (2005) 279–390, [hep-ph/0404175].

[5] S. D. M. White and M. J. Rees, *Core condensation in heavy halos: A Two stage theory for galaxy formation and clusters*, *Mon. Not. Roy. Astron. Soc.* **183** (1978) 341–358.

[6] **Planck** Collaboration, P. A. R. Ade et al., *Planck 2015 results. XIII. Cosmological parameters*, arXiv:1502.01589.

[7] C. Kilic, M. D. Klimek, and J.-H. Yu, *Signatures of Top Flavored Dark Matter*, *Phys.Rev.* **D91** (2015), no. 5 054036, [arXiv:1501.02202].

[8] P. Agrawal, S. Blanchet, Z. Chacko, and C. Kilic, *Flavored Dark Matter, and Its Implications for Direct Detection and Colliders*, *Phys. Rev.* **D86** (2012) 055002, [arXiv:1109.3516].

[9] K. Cheung, K. Mawatari, E. Senaha, P. Y. Tseng, and T. C. Yuan, *Top window for dark matter*, *Int. J. Mod. Phys.* **D20** (2011) 1413–1421.

[10] J. Kile and A. Soni, *Flavored Dark Matter in Direct Detection Experiments and at LHC*, *Phys. Rev.* **D84** (2011) 035016, [arXiv:1104.5239].

[11] B. Batell, J. Pradler, and M. Spannowsky, *Dark Matter from Minimal Flavor Violation*, *JHEP* **08** (2011) 038, [arXiv:1105.1781].

[12] J. F. Kamenik and J. Zupan, *Discovering Dark Matter Through Flavor Violation at the LHC*, *Phys. Rev.* **D84** (2011) 111502, [arXiv:1107.0623].

[13] A. Kumar and S. Tulin, *Top-flavored dark matter and the forward-backward asymmetry*, *Phys. Rev.* **D87** (2013), no. 9 095006, [arXiv:1303.0332].

[14] S. Chang, R. Edezhath, J. Hutchinson, and M. Luty, *Effective WIMPs*, *Phys. Rev.* **D89** (2014), no. 1 015011, [arXiv:1307.8120].

[15] J. Kile, *Flavored Dark Matter: A Review*, *Mod. Phys. Lett.* **A28** (2013) 1330031, [arXiv:1308.0584].

[16] Y. Bai and J. Berger, *Fermion Portal Dark Matter*, *JHEP* **11** (2013) 171, [arXiv:1308.0612].

[17] B. Batell, T. Lin, and L.-T. Wang, *Flavored Dark Matter and R-Parity Violation*, *JHEP* **01** (2014) 075, [arXiv:1309.4462].

[18] P. Agrawal, Z. Chacko, and C. B. Verhaaren, *Leptophilic Dark Matter and the Anomalous Magnetic Moment of the Muon*, *JHEP* **08** (2014) 147, [arXiv:1402.7369].

[19] P. Agrawal, B. Batell, D. Hooper, and T. Lin, *Flavored Dark Matter and the Galactic Center Gamma-Ray Excess*, *Phys. Rev.* **D90** (2014), no. 6 063512, [arXiv:1404.1373].

[20] M. A. Gomez, C. B. Jackson, and G. Shaughnessy, *Dark Matter on Top*, *JCAP* **1412** (2014), no. 12 025, [arXiv:1404.1918].

[21] P. Agrawal, M. Blanke, and K. Gemmler, *Flavored dark matter beyond Minimal Flavor Violation*, *JHEP* **1410** (2014) 72, [arXiv:1405.6709].

[22] A. Hamze, C. Kilic, J. Koeller, C. Trendafilova, and J.-H. Yu, *Lepton-Flavored Asymmetric Dark Matter and Interference in Direct Detection*, *Phys. Rev.* **D91** (2015), no. 3 035009, [arXiv:1410.3030].

[23] C.-J. Lee and J. Tandean, *Lepton-Flavored Scalar Dark Matter with Minimal Flavor Violation*, *JHEP* **04** (2015) 174, [arXiv:1410.6803].

[24] J. Kile, A. Kobach, and A. Soni, *Lepton-Flavored Dark Matter*, *Phys. Lett.* **B744** (2015) 330–338, [arXiv:1411.1407].

[25] P. Agrawal, Z. Chacko, E. C. F. S. Fortes, and C. Kilic, *Skew-Flavored Dark Matter*, *Phys. Rev.* **D93** (2016), no. 10 103510, [arXiv:1511.06293].

[26] A. J. Buras, P. Gambino, M. Gorbahn, S. Jager, and L. Silvestrini, *Universal unitarity triangle and physics beyond the standard model*, *Phys. Lett.* **B500** (2001) 161–167, [hep-ph/0007085].

[27] G. D'Ambrosio, G. F. Giudice, G. Isidori, and A. Strumia, *Minimal flavor violation: An Effective field theory approach*, *Nucl. Phys.* **B645** (2002) 155–187, [hep-ph/0207036].

[28] A. J. Buras, *Minimal flavor violation*, *Acta Phys. Polon.* **B34** (2003) 5615–5668, [hep-ph/0310208].

[29] M.-C. Chen, J. Huang, and V. Takhistov, *Beyond Minimal Lepton Flavored Dark Matter*, *JHEP* **02** (2016) 060, [arXiv:1510.04694].

[30] M. Blanke, A. J. Buras, A. Poschenrieder, S. Recksiegel, C. Tarantino, S. Uhlig, and A. Weiler, *Another look at the flavour structure of the littlest Higgs model with T-parity*, *Phys. Lett.* **B646** (2007) 253–257, [hep-ph/0609284].

[31] M. Papucci, A. Vichi, and K. M. Zurek, *Monojet versus the rest of the world I: t-channel models*, *JHEP* **11** (2014) 024, [arXiv:1402.2285].

[32] T. Hurth and W. Porod, *Flavour violating squark and gluino decays*, *JHEP* **08** (2009) 087, [arXiv:0904.4574].

[33] M. Blanke, G. F. Giudice, P. Paradisi, G. Perez, and J. Zupan, *Flavoured Naturalness*, *JHEP* **06** (2013) 022, [arXiv:1302.7232].

[34] P. Agrawal and C. Frugiuele, *Mixing stops at the LHC*, *JHEP* **01** (2014) 115, [arXiv:1304.3068].

[35] M. Arana-Catania, S. Heinemeyer, and M. J. Herrero, *Updated Constraints on General Squark Flavor Mixing*, *Phys. Rev.* **D90** (2014), no. 7 075003, [arXiv:1405.6960].

[36] M. Backović, A. Mariotti, and M. Spannowsky, *Signs of Tops from Highly Mixed Stops*, *JHEP* **06** (2015) 122, [arXiv:1504.00927].

[37] M. Blanke, B. Fuks, I. Galon, and G. Perez, *Gluino Meets Flavored Naturalness*, *JHEP* **04** (2016) 044, [arXiv:1512.03813].

[38] **ATLAS** Collaboration, G. Aad et al., *Search for top squark pair production in final states with one isolated lepton, jets, and missing transverse momentum in $\sqrt{s}$ =8 TeV pp collisions with the ATLAS detector*, *JHEP* **11** (2014) 118, [arXiv:1407.0583].

[39] **ATLAS** Collaboration, G. Aad et al., *Search for squarks and gluinos with the ATLAS detector in final states with jets and missing transverse momentum using $\sqrt{s} = 8$ TeV proton–proton collision data*, *JHEP* **09** (2014) 176, [arXiv:1405.7875].

[40] A. Alloul, N. D. Christensen, C. Degrande, C. Duhr, and B. Fuks, *FeynRules 2.0 - A complete toolbox for tree-level phenomenology*, *Comput. Phys. Commun.* **185** (2014) 2250–2300, [arXiv:1310.1921].

[41] J. Alwall, M. Herquet, F. Maltoni, O. Mattelaer, and T. Stelzer, *MadGraph 5 : Going Beyond*, *JHEP* **06** (2011) 128, [arXiv:1106.0522].

[42] A. J. Buras, S. Jäger, and J. Urban, *Master formulae for $\Delta F = 2$ NLO QCD factors in the standard model and beyond*, *Nucl. Phys.* **B605** (2001) 600–624, [hep-ph/0102316].

[43] S. Aoki, Y. Aoki, C. Bernard, T. Blum, G. Colangelo, et al., *Review of lattice results concerning low-energy particle physics*, *Eur.Phys.J.* **C74** (2014) 2890, [arXiv:1310.8555].

[44] N. Carrasco, M. Ciuchini, P. Dimopoulos, R. Frezzotti, V. Gimenez, et al., *$D^0-\bar{D}^0$ mixing in the standard model and beyond from N_f =2 twisted mass QCD*, *Phys.Rev.* **D90** (2014), no. 1 014502, [arXiv:1403.7302].

[45] **LHCb** Collaboration, R. Aaij et al., *Precision measurement of D meson mass differences*, *JHEP* **1306** (2013) 065, [arXiv:1304.6865].

[46] **UTfit Collaboration** Collaboration, A. Bevan et al., *The UTfit collaboration average of D meson mixing data: Winter 2014*, *JHEP* **1403** (2014) 123, [arXiv:1402.1664].

[47] G. Steigman, B. Dasgupta, and J. F. Beacom, *Precise Relic WIMP Abundance and its Impact on Searches for Dark Matter Annihilation*, *Phys.Rev.* **D86** (2012) 023506, [arXiv:1204.3622].

[48] J. D. Wells, *Annihilation cross-sections for relic densities in the low velocity limit*, hep-ph/9404219.

[49] K. Griest and D. Seckel, *Three exceptions in the calculation of relic abundances*, *Phys. Rev.* **D43** (1991) 3191–3203.

[50] G. Servant and T. M. P. Tait, *Is the lightest Kaluza-Klein particle a viable dark matter candidate?*, *Nucl. Phys.* **B650** (2003) 391–419, [hep-ph/0206071].

[51] D. S. Akerib et al., *Results from a search for dark matter in the complete LUX exposure*, arXiv:1608.07648.

[52] **PandaX-II** Collaboration, A. Tan et al., *Dark Matter Results from First 98.7 Days of Data from the PandaX-II Experiment*, *Phys. Rev. Lett.* **117** (2016), no. 12 121303, [arXiv:1607.07400].

[53] **XENON** Collaboration, S. Diglio, *XENON1T: the start of a new era in the search for Dark Matter*, *PoS* **DSU2015** (2016) 032.

[54] **LZ** Collaboration, D. S. Akerib et al., *LUX-ZEPLIN (LZ) Conceptual Design Report*, arXiv:1509.02910.

[55] **DARWIN** Collaboration, J. Aalbers et al., *DARWIN: towards the ultimate dark matter detector*, *JCAP* **1611** (2016), no. 11 017, [arXiv:1606.07001].

[56] J. L. Feng, J. Kumar, and D. Sanford, *Xenophobic Dark Matter*, *Phys. Rev.* **D88** (2013), no. 1 015021, [arXiv:1306.2315].